

Article

# Experimental Verification of Statistically Optimized Parameters for Low-Pressure Cold Spray Coating of Titanium

Damilola Isaac Adebisi<sup>1,2,\*</sup>, Abimbola Patricia Popoola<sup>1,\*</sup> and Ionel Botef<sup>3</sup>

<sup>1</sup> Department of Chemical, Metallurgical and Materials Engineering, Tshwane University of Technology, P.M.B. X680, Pretoria 0001, South Africa

<sup>2</sup> Department of Metallurgical Engineering, Vaal University of Technology, Vanderbijlpark 1911, South Africa

<sup>3</sup> School of Mechanical, Industrial and Aeronautical Engineering, University of the Witwatersrand, Johannesburg 2000, South Africa; ionel.botef@wits.ac.za

\* Correspondence: adebiyidi@vut.ac.za (D.I.A.); PopoolaAPI@tut.ac.za (A.P.P.);  
Tel.: +27-(0)16-950-7629 (D.I.A.); +27-(0)12-382-3513 (A.P.P.)

Academic Editor: Soran Biroasca

Received: 19 April 2016; Accepted: 24 May 2016; Published: 2 June 2016

**Abstract:** The cold spray coating process involves many process parameters which make the process very complex, and highly dependent and sensitive to small changes in these parameters. This results in a small operational window of the parameters. Consequently, mathematical optimization of the process parameters is key, not only to achieving deposition but also improving the coating quality. This study focuses on the mathematical identification and experimental justification of the optimum process parameters for cold spray coating of titanium alloy with silicon carbide (SiC). The continuity, momentum and the energy equations governing the flow through the low-pressure cold spray nozzle were solved by introducing a constitutive equation to close the system. This was used to calculate the critical velocity for the deposition of SiC. In order to determine the input temperature that yields the calculated velocity, the distribution of velocity, temperature, and pressure in the cold spray nozzle were analyzed, and the exit values were predicted using the meshing tool of Solidworks. Coatings fabricated using the optimized parameters and some non-optimized parameters are compared. The coating of the CFD-optimized parameters yielded lower porosity and higher hardness.

**Keywords:** process parameters; cold spray; optimization; critical velocity; SiC; microstructure; properties

## 1. Introduction

Ti-6Al-4V is an alloy of titanium that is characterized by excellent bulk mechanical and chemical properties such as very good strength-to-weight ratio (due to low density), high specific strength, low elastic modulus, superior resistance to both corrosion and erosion in many environments, excellent high temperature resistance, and biocompatibility. Hence, the alloy is a favorite material for many applications in the automobile, aerospace, and aeronautical industries. It would have found more versatile applications in these industries were it not for its poor surface properties such as hardness and wear resistance which are due to the high friction coefficient, low hardenability, and the tendency to gall and smear [1]. These poor surface properties are traced to the low resistance to plastic shearing, low work hardening, and the low protection offered by its surface oxide [2]. The aforementioned setback of titanium alloy has necessitated various research works, including coating with powder, to enhance the surface properties and performance without altering the bulk composition/chemistry thereby retaining the excellent bulk properties [3].

Silicon carbide (SiC), due to its extreme hardness and high wear resistance [4], is one of such powders for coating titanium alloy in order to confer higher hardness and wear resistance on it.

However, SiC decomposes before melting [5] making high temperature coating processes unsuitable for its deposition. A promising option to high temperature deposition of SiC that will prevent its thermal decomposition is the cold spray process. Cold spray is a material deposition process in which relatively small particles (ranging from approximately 5 to 100  $\mu\text{m}$  in diameter) in solid state are accelerated to a critical high velocity (typically 300–1400 m/s), and are subsequently plastically deformed to form a coating on the substrate [6,7]. In cold spray coating, attachment of powder to the substrate otherwise known as bonding is achieved by the kinetic energy of the powder particles rather than the thermal energy as the case in thermal spray processes [8]. Therefore, the fabrication of the coating of temperature sensitive and nano-structured material is possible by cold spray because no significant change in the microstructure of feedstock is involved in the process [9]. Bonding takes place when the velocity of the powder particles exceeds a certain value called the critical velocity (CV). Hence, the CV is defined as the velocity the particle must attain before deposition can take place after impacting the substrate [10]. The CV is a major parameter in cold spray; it is related to the mechanical and thermal properties of the spray materials and their particle sizes, and it determines which of particle deposition or substrate erosion will occur upon the impact of spray particles [11,12].

Typically, the CV is the velocity at which the transition from erosion of the substrate to deposition of the particle takes place [11]. Below the critical velocity, plastic deformation is too low to cause bonding, above the critical velocity, hydrodynamic penetration leads to strong erosion. Therefore, the optimum conditions for deposition lie between these two characteristic velocities [13]. According to Assadi [14], the value of CV is determined by the temperature, thermo-mechanical properties of the sprayed material [15] and the characteristics of the substrate [13,16,17]. Li *et al.* [18] measured the critical velocity for three metal alloys at different oxidizing conditions. The results showed that besides materials properties, the critical velocity was significantly influenced by the oxidation condition of the particles. The authors concluded that the material's properties influence the critical velocity more remarkably at low oxygen content than at high oxygen content. Yokoyama *et al.* [19] carried out the analysis of a metal particle impacting onto a metal substrate by using a dynamic finite element code (ABAQUS), and numerically studied the effects of substrate and particle temperature on the critical velocity. It was found that critical velocity decreases with higher stiffness of the substrate, higher particle temperature, and greater particle size. A decrease in gas temperature and pressure also affects coatings density and structure [20]. Li *et al.* [21] carried out both experimental and theoretical estimates of the critical velocity of copper (Cu) particles during cold spray coating. The authors concluded that the measured critical velocity was independent of the size and velocity distribution of the particle but depends on its temperature. Hence, in order to predict quality of the coating in cold spray, a good understanding of the particle velocity is vital.

Cold spray coating is carried out in a de Laval nozzle of which two variants are currently commercially available, *viz.*: the Low Pressure Cold Spray (LPCS) system and the High Pressure Cold Spray (HPCS) system. Inside the nozzle, the flow of high-velocity gas carrying very fine solid particles leads to a two-phase flow of gas-solid suspension. Such flow is usually extremely complex and difficult to understand due to the complexities arising mainly from particle-mean stream interactions, particle-flow turbulence interactions, inter-particle collisions, particle-wall interactions, and particle-shock wave interactions [22]. Dmitrienko and Uvarova [23] reported that mathematical modeling of heat and mass transfer in systems of dispersed particles, nano-particles, and nano-fluids, as in the cold spray nozzle, is one of the actual problems at present.

According to Vutova and Donchev [24], computational modeling and optimization are important for better process studying and understanding, and for quality improvement. Although few literatures are available on mathematical study and optimization of cold spray process parameters [18,19,21], as far as the authors of this work are aware, Computational Fluid Dynamics (CFD) analysis of input temperature to determine the critical velocity, which is the object of this investigation, has not been reported in the literature. The investigation consists of the following parts: (1) statistical computation of the critical velocity for cold spray coating of titanium alloy with SiC. This was done by using

a constitutive equation to solve the continuity, momentum, and energy equations governing the flow of fluid inside the de Lava nozzle used in the LPCS system; (2) Computational fluid dynamics (CFD) analysis of the flow through the nozzle to determine the input temperature that will yield the computed velocity at the exit of the nozzle; and (3) verification of the mathematical model by comparing the properties of coatings deposited using the CFD-optimized parameters and some non-optimized parameters.

## 2. Mathematical Modeling

The low Pressure Cold Spray (LPCS) system is shown in Figure 1. The basic principle of the cold spray involves a high-velocity flow of the particles made possible by the high pressure and high velocity of the carrier gas. The high pressure jet is preheated to compensate for the adiabatic cooling due to expansion. The powder particles are transported by the energy of the preheated, high-pressure, high-velocity supersonic gas jet.

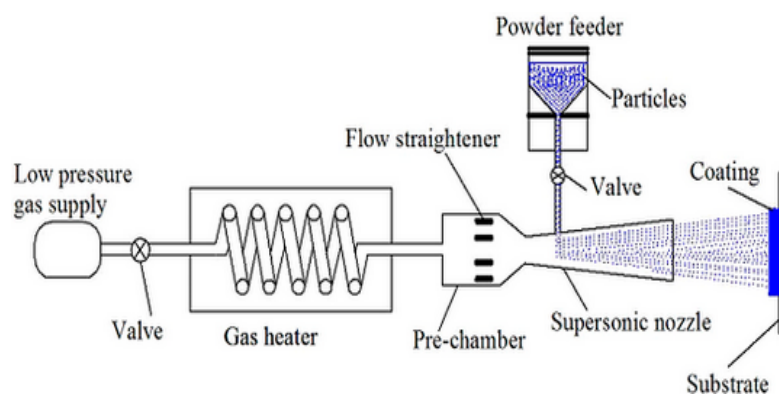


**Figure 1.** Schematic diagram of the low-pressure cold spray process [25].

### 2.1. Modeling Assumptions

In formulating this model, it is assumed that:

- (1) Ideal gas law is obeyed by the carrier gas.
- (2) The gas flow is one-dimensional, frictionless, and adiabatic.
- (3) Steady-state conditions exist.
- (4) Gas expansion is uniform; no shocks or discontinuities.
- (5) Particles effect on gas conditions is negligible.
- (6) Inter-particle collision is negligible.
- (7) Particles effect on space charge is negligible.

### 2.2. Model Equations

According to Papyrin [26], Lee *et al.* [27] and Janzhong *et al.* [28], the flow through the nozzle in the LPGDS process is governed by the continuity, momentum and the energy equations. A constitutive equation is however required in order to close the system.

#### 2.2.1. The Continuity Equation

A continuity equation is an equation that describes the transport of a conserved quantity. According to the continuity equation (otherwise known as the law of conservation of mass), the rate at which mass enters a system is equal to the rate at which mass leaves the system in any steady state process, *i.e.*, the total time rate of change of mass in a fixed region is zero. Therefore, the mass,

energy and momentum of the powder in the gas stream are conserved. The continuity equation for the LPCS can be written as:

$$\frac{\partial \rho}{\partial t} + \frac{\partial (\rho v_i)}{\partial x_i} = 0 \quad (1)$$

where  $\rho$  is the density of the gas and  $v$  is the velocity.

### 2.2.2. The Momentum Equation

According to Chuayjan *et al.* [29], one of the governing equations describing the motion of a particle in the LPCS system is the principle of linear momentum. The principle states that the total momentum of a system of colliding objects remains constant provided no resultant external force acts on the system. In other words, when no external forces are acting, the time rate of change of the momentum is equal to the net force acting on the particle. Taking internal stress and the gravitational acceleration into account, the application of principle of conservation of translational momentum for the LPCS can be written as:

$$\frac{\partial \rho v_i}{\partial t} + \frac{\partial (\rho v_j v_i)}{\partial x_j} = \frac{\partial \tau_{ij}}{\partial x_j} - \frac{\partial p}{\partial x_i} + \rho g \quad (2)$$

$\tau$  is the internal stress and  $g$  is the gravitational acceleration.

### 2.2.3. The Energy Equation

The kinetic energy of the particles on impact is important for plastic deformation of the particles and formation of splats, which bond together to produce coatings. The energy equation is given in Equation (3):

$$\frac{\partial (\rho E)}{\partial t} + \frac{\partial (\rho v_j E)}{\partial x_j} = \frac{\partial}{\partial x_j} \left( k \frac{\partial T}{\partial x_j} \right) + \frac{\partial}{\partial x_j} (\tau_{ij} v_i) \quad (3)$$

### 2.2.4. The Constitutive Equation

Constitutive equations relate thermo-mechanical parameters, *i.e.*, strain ( $\epsilon$ ), strain rate ( $\dot{\epsilon}$ ), temperature ( $T$ ), and flow stress ( $\sigma$ ). Although the conserved quantitative (mass, momentum, and energy) are the basic quantities describing the flow through the LPCS system, in order to close the system, a constitutive equation is required for stress and flow/flux, otherwise stress and flow must be added to the list of variable. Equations (1)–(3) are solved in conjunction with an appropriate equation of state and the constitutive equation. The stress equation for Newtonian fluid is given by Equation (4):

$$\tau_{ij} = \mu \left[ \left( \frac{\partial v_i}{\partial x_j} + \frac{\partial v_j}{\partial x_i} \right) - \frac{2\partial v_k}{3\partial x_k} \right] \quad (4)$$

where  $i, j = (x, y, z)$ .

The total stress tensor  $\sigma_{ij}$  in the fluid is given by the sum of internal stresses due to the fluid pressure  $p$  and the stress due to viscous forces as shown in Equation (5):

$$\sigma_{ij} = -p\delta_{ij} + \tau_{ij} \quad (5)$$

where  $\delta_{ij}$  is the Kronecker delta, defined such that  $\delta_{ij} = 1$  if  $i = j$ , otherwise  $\delta_{ij} = 0$ .

### 2.2.5. The Discrete Equations

The discrete approximation to the momentum, energy, and continuity equations can be written in a form shown in Equations (6) and (7):

$$Mu + A(u)u + GP = Ku + f(t) \quad (6)$$

$$Du = g(t) \quad (7)$$

$M$ —Mass matrix (for equidistant discretization of the unit matrix),  $A$ —advection matrix,  $G$ —gradient matrix,  $K$ —diffusion matrix,  $D$ —divergence matrix,  $f(t)$  and  $g(t)$  represents the effects of the boundary conditions on velocity.

Using the notations and equalities in Equation (8), and If  $G$  is denoted with  $C$ , Equation (9) is obtained:

$$b \equiv Ku + f(t) - A(u)u, D \equiv G^T \quad (8)$$

$$\begin{bmatrix} M & C \\ C^T & 0 \end{bmatrix} \begin{bmatrix} P \\ u \end{bmatrix} = \begin{bmatrix} b \\ g \end{bmatrix} \quad (9)$$

Consequently, the discrete system for the constitutive equation is obtained as shown in Equation (10) whereas that of the momentum, energy, and continuity equations are represented as shown in Equation (11) [30]:

$$\begin{bmatrix} N & 0 & 0 \\ 0 & N & 0 \\ 0 & 0 & N \end{bmatrix} \begin{bmatrix} \tau_{11} \\ \tau_{22} \\ \tau_{12} \end{bmatrix} - \begin{bmatrix} 2L_1 & 0 & 0 \\ 0 & 2L_2 & 0 \\ 0 & 0 & 0 \end{bmatrix} \begin{bmatrix} V_i \\ V_j \\ P \end{bmatrix} + \begin{bmatrix} D_1 & 0 & 0 \\ 0 & D_2 & 0 \\ 0 & 0 & 0 \end{bmatrix} \begin{bmatrix} V_i \\ V_j \\ P \end{bmatrix} = \begin{bmatrix} 0 \\ 0 \\ 0 \end{bmatrix} \quad (10)$$

$$\begin{bmatrix} c_i u_i & 0 & 0 \\ 0 & c_i u_i & 0 \\ 0 & 0 & 0 \end{bmatrix} \begin{bmatrix} V_i \\ V_j \\ P \end{bmatrix} + \begin{bmatrix} 2K_{11} + 2K_{22} & K_{21} & Q_1 \\ K_{22} & 2K_{11} + 2K_{22} & Q_2 \\ Q_1^T & Q_2^T & 0 \end{bmatrix} \begin{bmatrix} V_i \\ V_j \\ P \end{bmatrix} = \begin{bmatrix} F_1 \\ F_2 \\ 0 \end{bmatrix} \quad (11)$$

Equation (11) is solved by using Continuum mechanics.

The finite element equation for the flow process can be written by defining the coefficient matrix as given in Equations (12)–(19) [30].

$$\begin{bmatrix} C_i U_i(V_i) \\ C_i V_i(V_j) \\ 0 \end{bmatrix} + \begin{bmatrix} (2K_{11} + K_{22})V_i - K_{21}(V_j) + Q_1 P \\ -K_{22}(V_i) + K_{11} + 2K_{22}(V_j) - Q_2 P \\ Q_1^T(V_i) - Q_2^T(V_j) + 0 \end{bmatrix} = \begin{bmatrix} F_1 \\ F_2 \\ 0 \end{bmatrix} \quad (12)$$

$$C_i U_i(V_i) - C_i U_i(V_j) + \begin{bmatrix} (2K_{ij} + K_{ij})V_i - K_{ij}(V_j) + Q_i P \\ -K_{ij}(V_i) + K_{ij} + 2K_{ij}(V_j) - Q_i P \\ Q_i^T(V_i) - Q_i^T(V_j) + 0 \end{bmatrix} = \begin{bmatrix} F_1 \\ F_2 \\ 0 \end{bmatrix} \quad (13)$$

$$C_i U_i(V_i - V_j) + \begin{bmatrix} 3K_{ij}V_i - K_{ij}(V_j) + Q_i P \\ -K_{ij}(V_i) + K_{ij} + 2K_{ij}(V_j) - Q_i P \\ Q_i^T(V_i) - Q_i^T(V_j) + 0 \end{bmatrix} = \begin{bmatrix} F_1 \\ F_2 \\ 0 \end{bmatrix} \quad (14)$$

Taken  $(V_i - V_j) = U$ , then Equation (15) is obtained:

$$C_i U_i + \begin{bmatrix} + \\ - \\ + \end{bmatrix} \begin{bmatrix} 2K_{ij}(U) + Q_i P \\ K_{ij}(1 + U) - Q_i P \\ Q_i^T(U) \end{bmatrix} = \begin{bmatrix} F_1 \\ F_2 \\ 0 \end{bmatrix} \quad (15)$$

$$C_i U_i + (2K_{ij}U - K_{ij}U + Q_i^T(U)) = F_i \quad (16)$$

$$C_i U_i + (K_{ij} U + Q_i^T(U)) = F_i \quad (17)$$

$$C_i U_i + (K_{ij} U + Q_i^T(U)) = F_i \quad (18)$$

$$F_i = C U + K_{ij} U + Q_i^T U \quad (19)$$

Thus, the finite element Equations (10) and (11) become Equations (20) and (21):

$$C_{(u)} + K U = F \quad (20)$$

$$N_\tau - L U + D U = 0 \quad (21)$$

Equation (20) is the typical form of the Newtonian equation whereas Equation (21) represents the extra stress finite element analogue of the constitutive equation described in Section 2.2.4. These equations are solved by substituting the boundary conditions in Table 1. The exit velocity was calculated from Equation (20).

**Table 1.** Thermo mechanical properties of the carrier gas (air) and the silicon carbide (SiC) powder.

Carrier Gas (Air)		SiC Powder	
Density	1.205 kg/m <sup>3</sup>	Density	3160 kg/m <sup>3</sup>
Specific heat capacity, $C_p$	1.005 J/kg·K	Heat capacity, $C$	675 J·kg <sup>-1</sup> ·K <sup>-1</sup>
Thermal conductivity, $h$	0.0257 W/m·K	Thermal conductivity	490 W·m <sup>-1</sup> ·K <sup>-1</sup>
Kinematic viscosity, $\nu$	15.11 × 10 <sup>-6</sup> m <sup>2</sup> /s	Elastic modulus, $E$	570 MPa
Expansion coefficient	3.43 × 10 <sup>-3</sup> 1/K	Poisson ratio, $\mu$	0.17
Prandtl's number, $P_r$	0.713		

### 2.3. Thermo-Physical Properties and Boundary Conditions

The boundary conditions are determined by the properties of the carrier gas and the feedstock powder. The carrier gas is air and the powder used in the calculation is SiC ceramic powder. The properties of the air and SiC are given in Table 1. The feedstock powder is at room temperature at inlet and its mass flow rate at room temperature is 10 g/min. At the outlet, the pressure of the nozzle,  $u = v = w = 0$ .

According to Lupoi [31], the supersonic nozzle is a critical component for the cold spray coating process. Lee *et al.* [32] reported that nozzle optimization is crucial to minimizing shock loss. Figure 2 shows the geometry of the nozzle whose parameters are in shown in Table 2.

**Table 2.** Geometrical parameters of the nozzle.

Section of the Nozzle	(mm)
Throat diameter	4
Nozzle entrance diameter	8
Nozzle exit diameter	6
Length of converging section	50
Length of diverging section	125

Successful bonding of feedstock powder particle to the substrate demands that the particle must exceed a critical velocity, which is a function of the thermo-mechanical properties of the powder and the substrate [7–13]. Basically, the velocity of the particle is always less than that of the carrier gas. Therefore, the velocity of the carrier gas must be substantially above the critical velocity for deposition of high quality coating [18]. Li *et al.* [33] reported that particle temperature affects critical velocity.

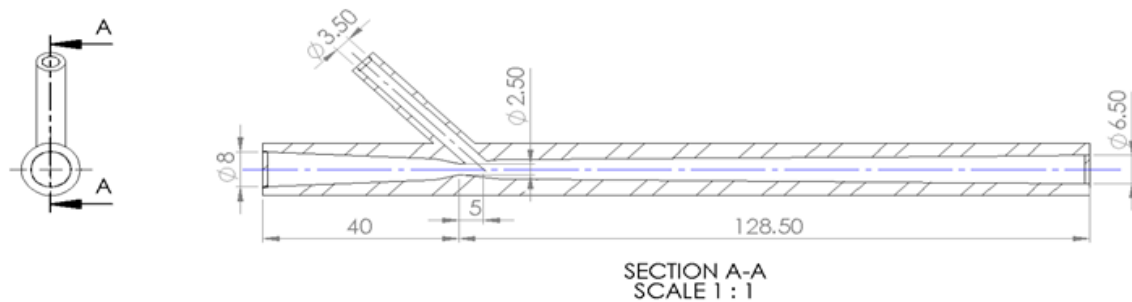


**Figure 2.** Geometry of the nozzle.

#### 2.4. Experimental Details

The feedstock powder used for this investigation consists of 95 wt. % SiC of 53  $\mu\text{m}$  particle size which was mechanically blended with 5 wt. % Al (Centerline SST-Al5001, CenterLine Limited, Windsor, ON, Canada) in a planetary ball mill. The addition of Al is necessary to act as a binder because SiC is a ceramic powder with limited plastic deformability. In order to simplify the mathematical model, the thermo-mechanical properties of Al are ignored. The weight percentage of Al is negligible as compared to SiC. Ti-6Al-4V with nominal composition: 6.10 wt. % Al, 4.01 wt. % V, 0.15 wt. % Fe, 0.007 wt. % C, 0.12 wt. % O, 0.005 wt. % N, Ti, balance and sectioned to  $35 \times 35 \times 5 \text{ mm}^3$  was used as the substrate. The substrates were grit blasted with 100–300  $\mu\text{m}$  alumina grit (Centerline SST-G0002, CenterLine Limited, Windsor, ON, Canada) prior to coating deposition. This is necessary to facilitate adhesion of the feedstock powder to the substrate. The cold spray coating experiment was performed with the Centreline SST Series P low pressure cold spray machine. The carrier gas was air generated by a 10 bar-capacity CompAir external air compressor. Centreline SST Series P is equipped with an automated gun moving device which was set at a transverse velocity of  $3 \text{ ms}^{-1}$ . Thus, it takes approximately 18 s to travel the 35 mm long substrate. Five passes were made on the substrate to form an approximate total thickness of 3 mm. A somewhat parabolic coating shape was observed. This suggests that the density of particle at the center of the nozzle is greater than that at the periphery. The powder was delivered axially into the pre-chamber of the nozzle in the supersonic gas stream by an integrated, dual-hopper, non-pressurized vibratory powder feeder at a feed rate set at 30%. Coating deposition was performed at the system's maximum allowable operational pressure of 0.99 MPa. This is because much higher pressure is usually required for the deposition of carbides during the cold spray coating [34]. There was no direct measurement of velocity at the exit of the nozzle but several values of temperature were simulated using the Solidworks Flow Simulation CFD package to determine their corresponding velocities at the exit of the nozzle.

To verify the accuracy of the set of simulated parameters, coatings were deposited using three temperatures and their properties were compared. Temperatures were selected based on the simulation results and preliminary investigations [35]. The temperatures are: (1) the CFD-optimized temperature (*i.e.*, the temperature whose output velocity agrees with the calculated velocity),  $T_{\text{opt}} = 773 \text{ K}$ ; (2)  $T_1 = 723 \text{ K}$  (50 K below  $T_{\text{opt}}$ ); and (3)  $T_2 = 823 \text{ K}$  (50 K above  $T_{\text{opt}}$ ).

After the coating process, the samples were sectioned, mounted, and polished semi-automatically to mirror finish following standard metallographic procedure [36]. X-ray diffraction analysis was performed on the coatings using the Philips P1710 Panalytical diffractometer (PANalytical, The Analytical X-ray Company, Almelo, The Netherlands) with Cu target  $K\alpha$  radiation to identify the constituent phases. The samples were scanned at intervals of  $2\theta$  and a step size of 0.02. The phases present were identified using X' Pert High score plus software (Version 2.2.2, PANalytical B.V., Almelo, The Netherlands). The structural data of the identified phases were taken from the ICSD database. The hardness measurements were performed on the prepared cross-section of the coating with a Vickers hardness tester (Future Tech FM-800, Version 1.15, Future Tech. Corp., Tokyo, Japan) according to ASTM E384 standard [37] to ensure consistent result. A load of 100 g was allowed to dwell for 15 s.

A total of ten indentations were made on each coating sample and the average is reported as the surface hardness of the sample. In order to avoid strain hardening effects and possible cracking of the reinforced matrix, indentations were spaced at a distance of at least four times the diagonal of the previous indent as per ASTM C1327 standard [38].

ImageJ analysis software (Version 1.48k, 2013, National Institute of Mental Health, Bethesda, MD, USA) was used to estimate the percentage porosity of coatings by calculating the area fraction of the pores. In order to cater for porosity at varied scale (micrometric, submicron, and nanometer pores) in the coatings, two different magnifications (1000× and 10,000×) of the SEM image were used. The work of Konečná *et al.* [39] agrees with this practice. The use of two different magnifications ensures that features like column gaps and big cracks will be captured by the lower magnification whereas features like sub-micrometric and nanometeric pores will be captured by the higher magnification [40]. Five micrographs were taken for each magnification. This is because a large number of micrograph at higher magnification may lead to a more reliable assessment of porosity. Although this method of image analysis may be cumbersome and time consuming, Ganvir *et al.* [40] reported it will provide an estimate of all types of pores such as connected, non-connected, vertical and branching cracks in the coating which may not be otherwise possible.

### 3. Results and Discussion

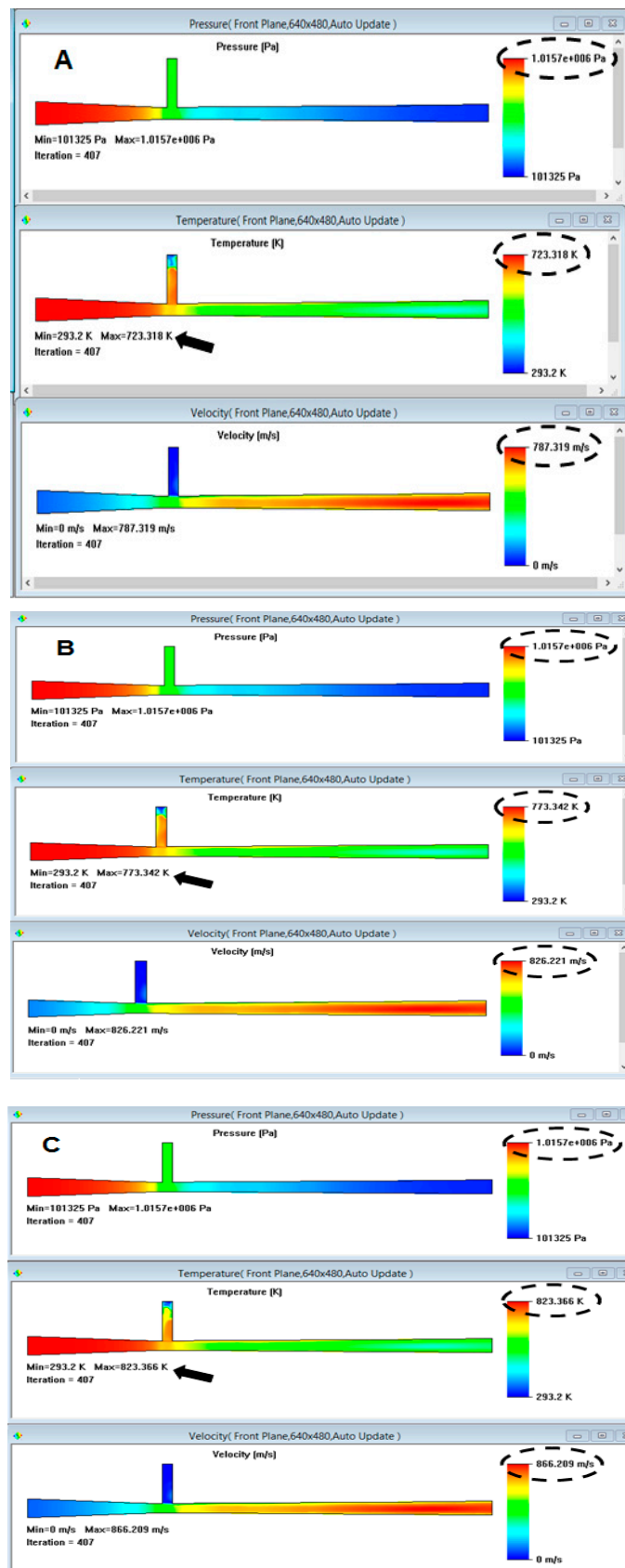
#### 3.1. Exit Velocity

Figure 3 shows the CFD analysis of gas flow in the nozzle for the three temperatures investigated. The distribution and exit values of velocity, temperature, and pressure are also shown in the Figure. The value of the velocity obtained from the mathematical calculation is in the range of that obtained from the CFD when the temperature is 500 °C (773 K). This is about 826 m/s as shown in Figure 3B. At 450 °C (723 K), the exit velocity is about 787 m/s (Figure 3A), whereas at 550 °C (823 K), the exit velocity is about 866 m/s (Figure 3C). According to the simulation result, Increase in input gas temperature led to increase in exit velocity. This is probably because, as shown in Equation (22), at a given mass flow rate, the velocity of the air increases as temperature increases [41]. This also confirms the work of Huang and Fukunuma [37], who reported that that higher gas temperature benefits impact velocity:

$$V_{\text{rms}} = \sqrt{\frac{3RT}{M}} \quad (22)$$

where,  $V_{\text{rms}}$  is the velocity,  $R$  is the universal gas constant,  $T$  is temperature, and  $M$  is mass.

Thus, a certain velocity range for efficient bonding and good coating properties called window of deposition has been defined. The window of deposition usually has both the minimum and maximum values. The minimum value is the critical velocity whereas the maximum value is called the erosion velocity. If the velocities of the particles are less than the critical velocity, there will be insufficient plastic deformation and no bonding. If the velocities of the particles are higher than critical velocity, there will be strong erosion as a result of hydrodynamic penetration. The optimum velocity for efficient deposition and good quality bonding lies between these two velocities [18]. The optimum velocity obtained from the statistical calculation is in good agreement with the value obtained from the CFD at temperature of 500 °C (773 K).



**Figure 3.** Computational fluid dynamics (CFD) predictions of the exit velocity for the three temperatures: (A) at  $T_1 = 723$  K, (B) at  $T_{opt} = 773$  K, and (C) at  $T_2 = 823$  K.

### 3.2. Microstructure and Porosity of the Coatings

The SEMs of the cross-section of the coatings are shown in Figure 4 whereas Figure 5 shows the XRD in relation to the feedstock powder.

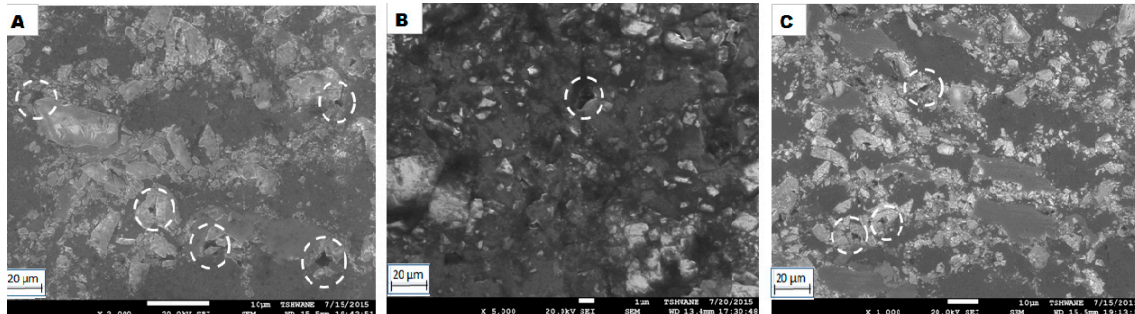


**Figure 4.** Scanning electron micrograph of the coatings: (A) 450 °C; (B) 500 °C; (C) 550 °C.

The micrographs of all the coatings are similar as they show partially homogenous distribution of SiC, and are generally characterized by fully dense structures and uneven surfaces. Although, no inter-connected pores are observed at any of the temperature investigated, a difference in porosity level is observed. The coating deposited using the CFD-optimized parameters yielded less porosity of 4.32% as compared to 5.05% and 4.97% respectively obtained at  $T_1$  and  $T_2$  (lower and higher than  $T_{opt}$ ). The lower porosity obtained from the optimized velocity is probably due to the hammering effect of the SiC particles on the coating which subsequently leads to a more dense structure. Higher velocity during cold spray coating usually leads to lower porosity.

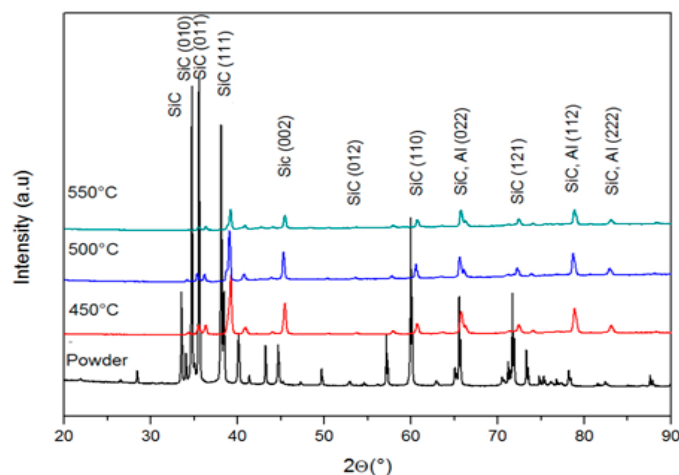


**Figure 5.** XRD of the coatings in comparison with the feedstock powder.

Huang and Fukunuma [42] observed that higher gas temperature benefits impact velocity and particle temperature, which leads to increase in the velocity of in-flight particles. Khalid [43] reported that impact energy is increased when the working gas temperature is increased. This increase in both the velocity of the in-flight particles and impact energy are expected to produce a decrease in volume fraction of porosity in the coatings. Thus the coating deposited at  $T_2$  is expected to yield less porosity than that deposited at  $T_{opt}$ . Contrarily, it is observed that at temperature above the optimized value, there is increase in percentage porosity of the coating. This is probably due to fracturing of the particles of SiC powder upon impact at higher velocity which will lead to increase in porosity. SiC is a ceramic powder; it is rigid and brittle, and higher impact velocity has the tendency to fracture it [44]. Moreover,

higher deposition temperature (and velocity) could have caused sufficient heat in the jetting region which could have aided thermal softening of the few Al particles in the feedstock powder. The increase in porosity at higher deposition temperature (and velocity) could also be because, at  $T_2$ , Al particles would have probably experienced thermal softening. Thermal softening causes reduced consolidation and increase porosity [42].

As shown in the XRD in Figure 5, there are no differences observed in the diffraction pattern of the coatings at the three temperatures investigated. This shows that the investigated temperature range has no effect on the phases formed in the coatings. Moreover, the diffraction patterns of the feed stock powder are identical to those of the coatings, although there is a noticeable peak shift between them. This peak shift could be traced to the high impact of the deposition process which would have caused micro-straining, amorphization and grain refinement of the powders particles.

### 3.3. Hardness of the Coatings

Although there is a general improvement in the surface hardness of the coatings, the sample deposited using the CFD-optimized parameter has the highest average hardness of  $652 \pm 12.7 \text{ HV}_{0.3}$  as compared to the  $599 \pm 14.8 \text{ HV}_{0.3}$ , and  $634 \pm 13.5 \text{ HV}_{0.3}$  respectively obtained at  $T_1$  and  $T_2$ . The general increase in hardness could be traced to the presence of hard SiC (Vickers hardness of 2350 [45]) particles in the feedstock powder, strain hardening effect of the plastically deformed Al particles during cold spray deposition, and accumulated strain caused by particle deformation during high impact blending and supersonic deposition processes.

Increase in velocity above the optimized value does not produce a corresponding increase in hardness of the coatings. The highest hardness was obtained from the optimized parameters and this is thought to be due to the lower porosity of its coating as explained in Section 3.2, and greater plastic deformation of Al particles at 500 °C. The greater the plastic deformation, the higher is the hardness [46]. Plastic deformation of Al particles will be higher at 500 °C than at 550 °C because thermal softening (which reduces plastic deformation) would have taken place at 550 °C since Al melts at 660 °C.

Ideally, as the gas temperature is increased, the average kinetic energy of the molecules of the gas will increase leading to increase in both particle temperature and impact velocity. This will produce corresponding increase in the momentum of the powder particles and greater particle impact, higher work hardening effect, greater coating densification, and increased coating hardness. However, the highest temperature does not produce the highest coating hardness. This is probably because the heat produced at the jetting regions at the higher deposition temperature would have favored dynamic recrystallization of Al particles which will lead to a reduction in hardness. Moreover, in addition to thermal softening explained above, the heat at the jetting region may also prevent sufficient plastic deformation of the Al, and consequently lessen strain hardening and hardness.

## 4. Conclusions

The continuity, momentum, and energy equations were solved by transforming the partial differential equations into a single ordinary differential equation. A constitutive equation was introduced to close the system, and also to account for stress and flow viscosity. The solution was used to calculate the optimum velocity for the deposition of SiC on titanium substrate using the LPCGD. CFD analysis of the flow through the nozzle was carried out to determine the input temperature that will yield the calculated velocity at the exit of the nozzle. Although there is no noticeable difference between the phases obtained in the coatings deposited with optimized and non-optimized parameters, coating with optimized parameter yielded less porosity and higher hardness. The higher hardness was traced to greater plastic deformation. Having established the relationship between the velocity, temperature, and pressure of the gas, for SiC, the solution can be used to predict these parameters for other powder materials by substituting the thermo-mechanical properties of the powder into the boundary conditions.

**Acknowledgments:** This material is based upon work supported financially by the National Research Foundation (NRF). The Cold Spray Laboratory of the University of Witwatersrand, Johannesburg is appreciated for the use of facilities. The authors also acknowledge the support from the African Laser Centre and the Tshwane University of Technology, Pretoria, South Africa which helped to accomplish this work.

**Author Contributions:** All authors contributed extensively to the work presented in this paper. A.P.P. and I.B. conceived the idea, supervised the work and revised the manuscript. D.I.A. performed the optimization, CFD analysis and experiments, analyzed and interpreted the data, and drafted the manuscript.

**Conflicts of Interest:** The authors declare no conflict of interest.

## Abbreviations

$\rho_g$	gas (air) density
$\delta_g$	Kronecker delta, which is a component of the identity tensor defined such that $\delta_{ij} = 1$ if $i = j$ , otherwise $\delta_{ij} = 0$
$\mathbf{v}$	velocity vector
$\tau$	stress tensor
$\mu$	molecular viscosity

## References

1. Adebisi, D.I.; Popoola, A.P.I.; Pityana, S.L. Phase constituents and microhardness of laser alloyed Ti-6Al-4V alloy. *J. Laser Appl.* **2015**, *27*, S29104. [[CrossRef](#)]
2. Adebisi, D.I.; Popoola, A.P.I. Mitigation of abrasive wear damage of Ti-6Al-4V by laser surface alloying. *Mater. Des.* **2015**, *74*, 67–75. [[CrossRef](#)]
3. Sahasrabudhe, H.; Soderlind, J.; Bandyopadhyay, A. Laser processing of *in situ* TiN/Ti composite coating on titanium. *J. Mech. Behav. Biomed. Mater.* **2016**, *53*, 239–249. [[CrossRef](#)] [[PubMed](#)]
4. Ravindra, D.; Patten, J. Ductile regime single point diamond turning of CVD-SiC resulting in an improved and damage-free surface. In Proceedings of the 4th International Conference on Recent Advances in Materials, Minerals & Environment and 2nd Asian Symposium on Materials & Processing, Penang, Malaysia, 1–3 June 2009.
5. Tului, M.; Giambi, B.; Lionetti, S.; Pulci, G.; Sarasini, F.; Valente, T. Silicon carbide based plasma sprayed coatings. *Surf. Coat. Technol.* **2012**, *207*, 182–189. [[CrossRef](#)]
6. Moridi, A.; Hassani-Gangaraj, S.M.; Guagliano, M.; Dao, M. Cold spray coating: Review of material systems and future perspectives. *Surf. Eng.* **2014**, *30*, 369–395. [[CrossRef](#)]
7. Villafuerte, J. Recent trends in cold spray technology: Looking at the future. *Surf. Eng.* **2010**, *26*, 393–394. [[CrossRef](#)]
8. Goyal, T.; Prince, S.; Walia, R.S.; Sidhu, T.S. Effect of nozzle geometry on exit velocity, temperature and pressure for cold spray process. *Int. J. Mat. Sci. Eng.* **2011**, *2*, 65–72.
9. Tria, S.; Elkedim, O.; Li, W.Y.; Liao, H. Ball milled Ni-Ti powder deposited by cold spraying. *J. Alloy. Compd.* **2009**, *483*, 334–336. [[CrossRef](#)]
10. Champagne, V. *The Cold Spray Materials Deposition Process: Fundamentals and Application*; Woodhead: Cambridge, UK, 2007.
11. Ghelichi, R.; Bagherifard, S.; Guagliano, M.; Verani, M. Numerical simulation of cold spray coating. *Surf. Coat. Technol.* **2011**, *205*, 5294–5301. [[CrossRef](#)]
12. Gartner, F. Advances in cold spraying. *Surf. Eng.* **2006**, *22*, 161–163. [[CrossRef](#)]
13. Schmidt, T.; Gartner, F.; Assadi, H.; Kreye, K. Development of a generalized parameter window for cold spray deposition. *Acta Mater.* **2006**, *54*, 729–742. [[CrossRef](#)]
14. Assadi, H.; Gartner, F.; Stoltenhoff, T.; Kreye, H. Bonding mechanism in cold gas spraying. *Acta Mater.* **2003**, *51*, 4379–4394. [[CrossRef](#)]
15. Alkimov, A.P.; Kosarev, V.E.; Papyrin, A.N. A method of cold gas-dynamic deposition. *Dokl. Akad. Nauk. SSSR* **1990**, *318*, 1062–1065.
16. Legoux, J.G.; Irissou, E.; Moreau, C. Effect of substrate temperature on the formation mechanism of cold-sprayed aluminum, zinc and tin coatings. *J. Therm. Spray Technol.* **2007**, *16*, 619–626. [[CrossRef](#)]
17. Gao, P.; Li, C.; Yang, C.; Li, Y.; Li, C. Influence of substrate hardness on deposition behavior of single porous WC-12Co particle in cold spraying. *Surf. Coat. Technol.* **2008**, *203*, 384–390. [[CrossRef](#)]

18. Li, C.J.; Wang, H.T.; Zhang, Q.; Yang, G.J.; Li, W.Y.; Liao, H.L. Influence of spray materials and their surface oxidation on the critical velocity in cold spraying. *J. Therm. Spray Technol.* **2010**, *19*, 95–101. [[CrossRef](#)]
19. Yokoyama, K.; Watanabe, M.; Kuroda, S.; Gotoh, Y.; Schmidt, T.; Gartner, F. Simulation of solid particle impact behaviour for spray processes. *J. Mater. Trans.* **2006**, *47*, 1697–1702. [[CrossRef](#)]
20. Henao, J.; Concustell, A.; Cano, I.G.; Cinca, N.; Dosta, S.; Guilemany, J.M. Influence of Cold Gas Spray process conditions on the microstructure of Fe-based amorphous coatings. *J. Alloy. Compd.* **2015**, *622*, 995–999. [[CrossRef](#)]
21. Li, C.J.; Li, W.Y.; Liao, H. Examination of the Critical Velocity for Deposition of Particles in Cold Spraying. *J. Therm. Spray Technol.* **2006**, *15*, 213. [[CrossRef](#)]
22. Sun, J.G.; Kim, H.D.; Park, J.O.; Jin, Y.Z. A Computational study of the gas-solid suspension flow through a supersonic nozzle. *Open J. Fluid Dyn.* **2012**, *2*, 242–247. [[CrossRef](#)]
23. Dmitrienko, G.S.; Uvarova, L.A. Modeling of dendritic growth in two dimensions. *Int. J. Pure Appl. Math.* **2013**, *82*, 663–668. [[CrossRef](#)]
24. Vutova, K.; Donchev, V. Electron beam melting and refining of metals: Computational modeling and optimization. *Materials* **2013**, *6*, 4626–4640. [[CrossRef](#)]
25. Goyal, T.; Sidhu, T.S.; Walia, R.S. Taguchi Based Optimization for Micro Hardness of Cold Spray Coating Process. *Intl. J. Surf. Eng. Interdiscip. Mat. Sci.* **2014**, *2*, 23–33. [[CrossRef](#)]
26. Papyrin, A.N. *Cold Spray: State of the Art and Applications*; Cold spray technology: Albuquerque, NM, USA, 2006; pp. 1–21.
27. Lee, J.C.; Kang, H.G.; Chu, W.S.; Ahn, W.S. Repair of damaged mold surface by cold-spray method. *CIRP Ann. Manuf. Technol.* **2007**, *56*, 577–580. [[CrossRef](#)]
28. Lin, J.; Ruan, X.; Chen, B. *Fluid Mechanics*; Tsinghua University Press: Beijing, China, 2005; pp. 72–91.
29. Chuayjan, W.; Pothiphan, S.; Wiwatanapataphee, B.; Wu, Y.H. Numerical simulation of granular flow during filling and discharging of a silo. *Int. J. Pure Appl. Math.* **2010**, *62*, 347–364.
30. Reddy, J.N.; Gartling, D.K. *The Finite Element Method in Heat Transfer and Fluid Dynamics*; CRC Press: London, UK, 1994.
31. Lupoi, R. Current design and performance of cold spray nozzles: Experimental and numerical observations on deposition efficiency and particle velocity. *Surf. Eng.* **2014**, *30*, 316–322. [[CrossRef](#)]
32. Lee, M.W.; Park, J.J.; Kim, D.Y.; Yoon, S.S.; Kim, H.Y.; Kim, D.H.; Park, D.S. Optimization of supersonic nozzle flow for titanium dioxide thin-film coating by aerosol deposition. *J. Aerosol. Sci.* **2011**, *42*, 771–780. [[CrossRef](#)]
33. Li, C.J.; Li, W.Y.; Liao, H. Examination of the critical velocity for deposition of particles in cold spraying. *J. Therm. Spray Technol.* **2006**, *15*, 212–222. [[CrossRef](#)]
34. Motta, F.V.; Balestra, R.M.; Ribeiro, S.; Taguchi, S.P. Wetting behaviour of SiC ceramics: Part I.  $E_2O_3/Al_2O_3$  additive system. *Mater. Lett.* **2004**, *58*, 2805–2809. [[CrossRef](#)]
35. Adebisi, D.I.; Botef, I.; Popoola, P.A. Computational technique for optimization of the process parameter for cold spray coating of titanium. In Proceedings of the 1st International Conference on Mathematical Methods & Computational Techniques in Science & Engineering, Athens, Greece, 28–30 November 2014; pp. 239–243.
36. Geels, K.; Fowler, D.B.; Kopp, W.U.; Ruckert, M. *Metallographic and Materialographic Specimen Preparation, Light Microscopy, Image Analysis, and Hardness Testing*; ASTM International: West Conshohocken, PA, USA, 2007.
37. ASTM Standard. E384-11E1, *Standard Test Method for Knoop and Vickers Hardness of Materials*; ASTM International: West Conshohocken, PA, USA, 2007. [[CrossRef](#)]
38. ASTM Standard. C1327, *Standard Test Method for Vickers Indentation Hardness of Advanced Ceramics*; ASTM International: West Conshohocken, PA, USA, 2008. [[CrossRef](#)]
39. Konecna, R.; Nicoletto, G.; Majerova, V. Largest extreme value determination of defect size with application to cast Al-Si alloys porosity. *Metal* **2007**, *16*, 94.
40. Ganvir, A.; Curry, N.; Bjorklund, S.; Markocsan, N.; Nylén, P. Characterization of Microstructure and Thermal Properties of YSZ Coatings Obtained by Axial Suspension Plasma Spraying (ASPS). *J. Therm. Spray Technol.* **2015**, *1*, 1–10. [[CrossRef](#)]
41. Moore, E.M.; Papavassiliou, D.V.; Shambaugh, R.L. Air velocity, air temperature, fiber vibration and fiber diameter measurements on a practical melt blowing die. *Int. Nonwovens J.* **2004**, *13*, 43–53.

42. Huang, R.Z.; Fukanuma, H. The Influence of Spray Conditions on Deposition Characteristics of Aluminum Coatings in Cold Spraying. In Proceedings of the International Thermal Spray Conference, 4–7 May 2009; Marple, B.R., Hyland, M.M., Lau, Y.-C., Eds.; Thermal Spray 2009: Las Vegas, Nevada, USA, 2009; pp. 279–284. [[CrossRef](#)]
43. Khalid, A.A. The effect of testing temperature and volume fraction on impact energy of composites. *Mater. Des.* **2006**, *27*, 499–506. [[CrossRef](#)]
44. Triantou, K.I.; Pantelis, D.I.; Guipont, V.; Jeandin, M. Microstructure and tribological behavior of copper and composite copper+alumina cold sprayed coatings for various alumina contents. *Wear* **2015**, *336*, 96–107. [[CrossRef](#)]
45. Medica, L.A. *Guidelines for Safe Handling of Powders and Bulk Solids*; Wiley: Hoboken, NJ, USA, 2004.
46. Smith, G.T. *Industrial Metrology: Surfaces and Roundness*; Springer Science & Business Media: New York, NY, USA, 2013; p. 202.



© 2016 by the authors; licensee MDPI, Basel, Switzerland. This article is an open access article distributed under the terms and conditions of the Creative Commons Attribution (CC-BY) license (<http://creativecommons.org/licenses/by/4.0/>).